ARL-TR-10440 • SEP 2026

Implementation of a Corner Theory Yield Surface Model Using a Novel Modulus Scaling Technique

by Richard Becker

NOTICES

Disclaimers

ARL-TR-10440 ● SEP 2026

Implementation of a Corner Theory Yield Surface Model Using a Novel Modulus Scaling Technique

Richard Becker
DEVCOM Army Research Laboratory

REPORT DOCUMENTATION PAGE

1. REPORT DATE	2. REPORT TYPE	3. DATES COVERED START DATE	END DATE
September 2026	Technical Report	1 February 2026	31 August 2026

4. TITLE AND SUBTITLE
Implementation of a Corner Theory Yield Surface Model Using a Novel Modulus Scaling Technique

5a. CONTRACT NUMBER	5b. GRANT NUMBER	5c. PROGRAM ELEMENT NUMBER
5d. PROJECT NUMBER	**5e. TASK NUMBER**	**5f. WORK UNIT NUMBER**

6. AUTHOR(S)
Richard Becker

7. PERFORMING ORGANIZATION NAME(S) AND ADDRESS(ES)	8. PERFORMING ORGANIZATION REPORT NUMBER
DEVCOM Army Research Laboratory ATTN: FCDD-RLA-TE Aberdeen Proving Ground, MD 21005	ARL-TR-10440

9. SPONSORING/MONITORING AGENCY NAME(S) AND ADDRESS(ES)	10. SPONSOR/MONITOR'S ACRONYM(S)	11. SPONSOR/MONITOR'S REPORT NUMBER(S)

12. DISTRIBUTION/AVAILABILITY STATEMENT
DISTRIBUTION STATEMENT A. Approved for public release: distribution unlimited.

13. SUPPLEMENTARY NOTES
ORCID: Richard Becker, 0000-0003-0104-856X

14. ABSTRACT
Closed-form integration of the J2-flow theory plasticity relation over a time step suggests a scaling of the shear modulus, which may be beneficial for integrating more challenging yield functions. The proposed scaling limits the elastic trial stress increment to less than the radius of the yield surface so that plastic return mapping along a prescribed path projects to a state on the yield surface. A numerical algorithm was developed and verified on a J2-flow theory model and was extended to a corner theory model, which has its plastic return path defined at the beginning of the time step. The algorithm proved stable and accurate on simple, nonproportional loading paths. Solutions were then obtained for right circular steel cylinders impacting finite aluminum targets. The corner theory results were similar to the J2-flow theory solution for initial penetration. As the penetrator neared the back surface, the corner theory model developed a clean cylindrical plug whereas the J2-flow model created a flared plug. Results were also obtained with a Tresca yield surface model for comparison.

15. SUBJECT TERMS
Tresca, corner theory, J2-flow, shear band, localization, plugging, Murnaghan, equation of state, Terminal Effects

16. SECURITY CLASSIFICATION OF: a. REPORT	b. ABSTRACT	C. THIS PAGE	17. LIMITATION OF ABSTRACT	18. NUMBER OF PAGES
UNCLASSIFIED	UNCLASSIFIED	UNCLASSIFIED	UU	44

19a. NAME OF RESPONSIBLE PERSON	19b. PHONE NUMBER *(Include area code)*
Richard Becker	520-853-0879

STANDARD FORM 298 (REV. 5/2020)
Prescribed by ANSI Std. Z39.18

Contents

List of Figures

List of Tables

1. Introduction

Fracture in many applications is preceded by strain localization where the focused plastic flow leads to thermal softening and/or accelerated damage. Simulating localization and subsequent fracture in continuum finite element codes requires that the material model readily admits strain localization and the numerical method freely accommodates it. Over the past half-century, there have been innumerable models and numerical algorithms proposed to predict strain localization and deal with it computationally (e.g., Rice 1976; Christoffersen and Hutchinson 1979; Triantafyllidis et al. 1982; Wright and Walter 1987; Fish and Belytschko 1988; Mourad et al. 2017; Margraf and Barton 2019).

Within the material constitutive description, two model components affect strain localization: strength relations and plastic flow rule. The plastic flow rule determines the ease by which the plastic flow can change direction, and the strength relations govern the thermal softening and stabilizing effects of strain hardening and rate sensitivity within a deforming shear band. Almost universally, high-rate simulations run at U.S. Army Combat Capabilities Development Command (DEVCOM) Army Research Laboratory (ARL) use J2-flow theory with an associative flow rule. In this model, the material yield surface is determined by the von Mises effective stress and the plastic flow direction is taken to be normal to this same function. This association between the yield surface and the plastic flow potential is not a requirement of plasticity theory (e.g., Hill 1950), but rather a choice made for both convenience and lack of data characterizing flow potentials.

Nonassociated plastic flow models, where the yield function and plastic flow potential differ, permit bifurcation from a uniform deformation state at positive work hardening rates (Rice 1976; Raniecki and Bruhns 1981). This is precluded for J2-flow theory with an associated flow potential. In the associated J2-flow model, the stress and plastic strain rate directions are coaxial, so the energy dissipated plastically is maximized. Maximum dissipation provides stability. In addition, the plastic flow direction and stress direction would have to change concurrently for a localized band to form, which imposes an additional constraint for associated J2-flow theory. For a nonassociated model, the directions of the yield surface normal and strain rate differ. The same deformation can occur with lower plastic dissipation, and the stress does not necessarily follow changes in strain rate direction. The solution has more freedom, which could facilitate strain localization.

Plastic flow potentials have been explored experimentally (e.g., Hecker 1976; Kuwabara et al. 2000) and computationally with crystal plasticity models (e.g., Kuroda and Tvergaard 2001a, Bassani and Racheria 2011). The experiments and computations are difficult and development of a plastic flow potential model for a full range of deformation conditions is intractable. However, the results tend to show a vertex, whereby the plastic flow is in the direction of the applied deformation without substantially altering the stress state. This observation has led to development of corner theory models like Christoffersen and Hutchinson (1979) and Simo (1987).

The corner theory models have been implemented and run successfully in research codes, but they are not available in codes used for ballistic simulations within the DoW. One reason for this is that the time step integration algorithm must be robust and accurate for strain increments tens of times larger than the yield strain. Such strain increments are common in ballistic calculations. The corner theory models are formulated using directional information from the beginning of the time step, and traditional algorithms can have convergence difficulties when using large strain increments and directions from the beginning of the time step.

A feature was recently observed in a closed-form solution for a J2-flow theory model that could be extended to facilitate integration of models utilizing information from the beginning of the time step. This report documents that finding and applies it to a corner theory model. The algorithm is implemented in a UMAT user material subroutine with an equation of state (EOS) and the Johnson–Cook strength and failure models. A ballistic penetration problem with plug formation is run to illustrate the applicability and utility of the model.

2. Model Formulation

2.1 Plastic Flow Integration Method

2.1.1 Basic J2-Flow Theory Relations

The rate form of the plasticity relations for isotropic J2-flow theory can be written as

$$\hat{\boldsymbol{\sigma}}' = 2\mu\, \boldsymbol{d}' - 3\mu\dot{\bar{\varepsilon}}\, \frac{\boldsymbol{\sigma}_t'}{\sigma_t^{vm}}\ , \tag{1}$$

where $\hat{\boldsymbol{\sigma}}'$ denotes an objective rate of the deviatoric part of the Cauchy stress tensor, μ is the shear modulus, $\boldsymbol{d}'$ is the deviatoric part of the rate of deformation tensor, and $\boldsymbol{\sigma}_t'$ is the deviatoric Cauchy stress at the beginning of the time increment. Scalars σ_t^{vm} and $\dot{\bar{\varepsilon}}$ are the von Mises equivalent stress and equivalent plastic strain rate, defined as

$$\sigma^{vm} = \sqrt{\frac{3}{2}\left(\boldsymbol{\sigma}' : \boldsymbol{\sigma}'\right)} \qquad \text{and} \qquad \dot{\bar{\varepsilon}} = \sqrt{\frac{2}{3}\left(\dot{\boldsymbol{\varepsilon}}'^{p} : \dot{\boldsymbol{\varepsilon}}'^{p}\right)}\,. \tag{2}$$

2.1.2 Manipulation of Closed-Form Expression

Assuming that the rotation of the stress increment is handled separately, the stress can be integrated over a time increment, Δt, for a constant deformation rate in a nonhardening material. This was accomplished using geometric arguments by Krieg and Krieg (1977) and a series solution is provided in the Appendix. The stress at the end of the time step from the Appendix is

$$\boldsymbol{\sigma}'_{t+\Delta t} = \exp\left(-\frac{3\mu\,\dot{\bar{\varepsilon}}\,\Delta t}{\sigma_t^{vm}}\right)\boldsymbol{\sigma}'_t + 2\mu\left(\frac{\sigma_t^{vm}}{3\mu\,\dot{\bar{\varepsilon}}\,\Delta t}\right)\left[1 - \exp\left(-\frac{3\mu\,\dot{\bar{\varepsilon}}\,\Delta t}{\sigma_t^{vm}}\right)\right]\boldsymbol{d}'\Delta t\,. \tag{3}$$

Consistent with the assumptions for the series solution, the von Mises effective stress is the quantity from the beginning of the time step, and the effective plastic strain rate is some averaged value over the time step. Implicit in the solution is that the state at the beginning of the time step is on the yield surface and further plastic deformation occurs over the strain increment. Initial stress states inside of the yield surface and strain increments that cause reverse loading through the yield surface are not represented. Equation 3 is the result of integrating a flow potential. It does not require that the stress satisfy any yield function.

Equation 3 can be rearranged as

$$\begin{aligned}\boldsymbol{\sigma}'_{t+\Delta t} = \boldsymbol{\sigma}'_t &+ 2\mu\left(\frac{\sigma_t^{vm}}{3\mu\,\dot{\bar{\varepsilon}}\,\Delta t}\right)\left[1 - \exp\left(-\frac{3\mu\,\dot{\bar{\varepsilon}}\,\Delta t}{\sigma_t^{vm}}\right)\right]\boldsymbol{d}'\,\Delta t \\ &- \left[1 - \exp\left(-\frac{3\mu\,\dot{\bar{\varepsilon}}\,\Delta t}{\sigma_t^{vm}}\right)\right]\boldsymbol{\sigma}'_t\end{aligned} \tag{4}$$

and further expansion yields

$$\begin{aligned}\boldsymbol{\sigma}'_{t+\Delta t} = \boldsymbol{\sigma}'_t &+ 2\mu\left(\frac{\sigma_t^{vm}}{3\mu\,\dot{\bar{\varepsilon}}\,\Delta t}\right)\left[1 - \exp\left(-\frac{3\mu\,\dot{\bar{\varepsilon}}\,\Delta t}{\sigma_t^{vm}}\right)\right]\boldsymbol{d}'\,\Delta t \\ &- \left(\frac{3\mu\,\dot{\bar{\varepsilon}}\,\Delta t}{\sigma_t^{vm}}\right)\left(\frac{\sigma_t^{vm}}{3\mu\,\dot{\bar{\varepsilon}}\,\Delta t}\right)\left[1 - \exp\left(-\frac{3\mu\,\dot{\bar{\varepsilon}}\,\Delta t}{\sigma_t^{vm}}\right)\right]\boldsymbol{\sigma}'_t\,.\end{aligned} \tag{5}$$

For convenience, a grouping of factors will be defined as

$$\mathcal{M} = \left(\frac{\sigma_t^{vm}}{3\mu\,\dot{\bar{\varepsilon}}\,\Delta t}\right)\left[1 - \exp\left(-\frac{3\mu\,\dot{\bar{\varepsilon}}\,\Delta t}{\sigma_t^{vm}}\right)\right] = \frac{1}{\mathcal{R}}\left[1 - \exp(-\mathcal{R})\right] \tag{6}$$

which results in the stress at the end of the time step being

$$\boldsymbol{\sigma}'_{t+\Delta t} = \boldsymbol{\sigma}'_t + 2\mu\, \mathcal{M}\, \boldsymbol{d}'\, \Delta t\ - 2\mu\, \mathcal{M}\, \dot{\bar{\varepsilon}}\, \Delta t\, \frac{3}{2} \frac{\boldsymbol{\sigma}'_t}{\sigma_t^{vm}}\ . \tag{7}$$

Equation 7 resembles the form for forward integration of the stress with $\mathcal{M}$ appearing in both time-incremented terms.

2.1.3 Implications of Strain Increment Scaling

$\mathcal{M}$ can be viewed as a scaling of the strain increment or, alternatively, as a scaling of the shear modulus. In Equation 6, the scaling factor is represented as a function of $\mathcal{R}$, which can be viewed as a multiple of the yield strain. A value of $\mathcal{R} = 2$ has a plastic strain increment twice that of the yield strain. $\mathcal{M}$ is plotted as a function of $\mathcal{R}$ in Figure 1. It begins at 1.0 for small plastic strain increments and it approaches $1/\mathcal{R}$ for values of $\mathcal{R}$ greater than 4.

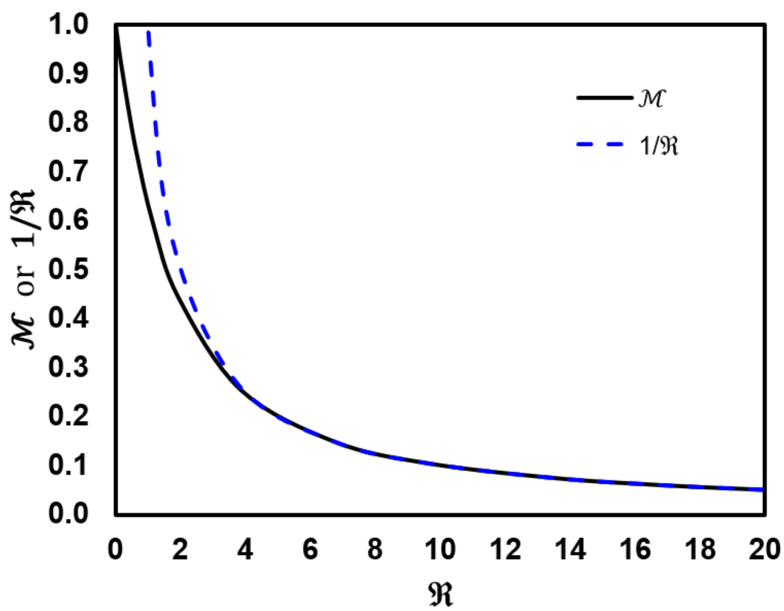

Figure 1. Strain increment scaling factor, $\mathcal{M}$, as a function of multiples of yield strain, $\mathcal{R}$.

The scaling by $\mathcal{M}$ is at the core of the proposed integration method. $\mathcal{M}$ is unity at infinitesimal strain increments, so Equation 7 is not changed from the traditional form in this limit. At large strain increments, such as 5 or 20 times the yield strain, both the total and the plastic strain increments are scaled by $\mathcal{M}$, such that the effective strain increments multiplying the shear modulus in Equation 7 are capped at the yield strain. In the context of yield surfaces in stress space, the elastic trial stress does not exceed one yield surface radius. Hence, the plastic return mapping to the yield surface along a specified direction is much less likely to miss the yield surface or go astray compared with return mapping from multiple yield surface diameters away. This is illustrated schematically in Figure 2. The proposed modulus reduction method could simplify existing algorithms and enable plasticity models that were impractical because of strain increment restrictions.

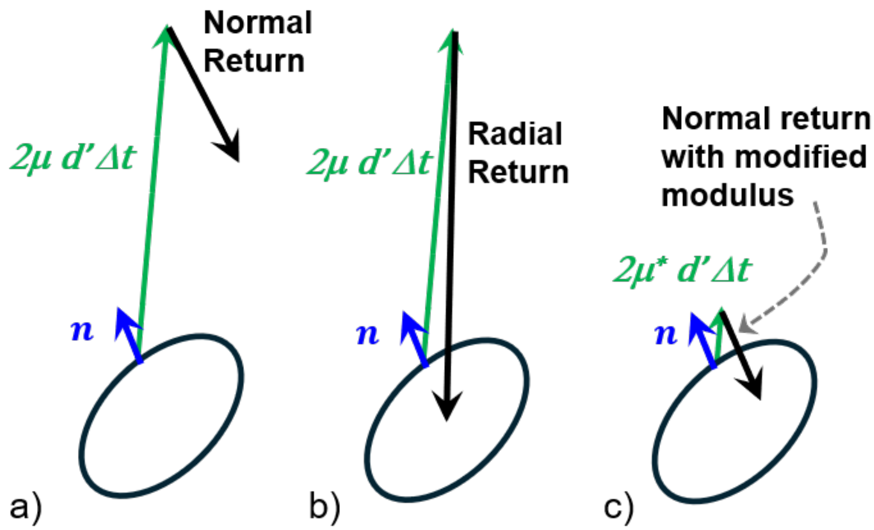

Figure 2. Illustration of the reduced-modulus algorithm for plastic return to the yield surface at finite strain increments. The trial stress increment in green is 6 times the yield stress and the normal at the loading point is in blue. The plastic return direction is the black arrow. a) For a simple forward-Euler method applied to Equation 7, a plastic return along the normal direction misses the yield surface. b) The radial return direction is guaranteed to hit the yield surface. c) The proposed reduced shear modulus creates a significantly smaller stress excursion, and plastic return parallel to the normal intersects the yield surface.

2.1.4 Computation of the Scaling Factor

The plastic strain rate is needed to compute $\mathcal{M}$. This estimate will be denoted $\dot{\epsilon}$. At large strain increments, the plastic strain increment cannot deviate significantly from the total strain increment, so an approximate plastic strain rate at large strain increments can be determined from the total rate of deformation tensor by

$$\dot{\epsilon}_{\mathrm{d}} = \sqrt{\tfrac{2}{3}(\boldsymbol{d}':\boldsymbol{d}')}\,. \tag{8}$$

For small strain increments and proportional loading in the plastic range, the plastic strain increment is also very close to the total strain increment. This is because the elastic part of the strain increment is related to the strength increase from strain hardening, and the stress increment from strain hardening at small strain increments is generally orders of magnitude lower than the flow strength. However, for nonproportional loading at modest strain increments, the total strain increment can be significantly larger than the plastic strain increment, particularly for an abrupt path change. For expedience in developing and evaluating the method, the plastic strain rate estimate at small strain increments is determined from a standard radial return solution, $\dot{\epsilon}_{rr}$. This is a redundant computational expense for a J2-flow theory model, but the ultimate intent is to apply the method to more complex flow models.

A transition is needed to go between the estimates at low and high strain increments. Here, the transition is a linear combination of the two estimated rates between $\mathcal{R}$ values of 1 and 2.

$$\dot{\epsilon} = \begin{cases} \dot{\epsilon}_{\mathrm{rr}}\,; & \text{for} \quad \dfrac{3\mu\,\dot{\epsilon}_{\mathrm{rr}}\,\Delta t}{\sigma_t^{vm}} < 1 \\ 2\,\dot{\epsilon}_{\mathrm{rr}} - \left(\dfrac{3\mu\,\dot{\epsilon}_{rr}\,\Delta t}{\sigma_t^{vm}}\right)(\dot{\epsilon}_{rr} - \dot{\epsilon}_d) - \dot{\epsilon}_d\,; & \text{for} \quad 1 \le \dfrac{3\mu\,\dot{\epsilon}_{\mathrm{rr}}\,\Delta t}{\sigma_t^{vm}} \le 2 \\ \dot{\epsilon}_{\mathrm{d}}\,; & \text{for} \quad 2 \le \dfrac{3\mu\,\dot{\epsilon}_{\mathrm{rr}}\,\Delta t}{\sigma_t^{vm}} \end{cases} \tag{9}$$

For nearly proportional loading, $\dot{\epsilon}_{\mathrm{rr}}$ and $\dot{\epsilon}_{\mathrm{d}}$ are only a few percent different, so the transition is usually negligible.

From a practical perspective, it is simpler to scale the shear modulus by $\mathcal{M}$ rather than the strain increment. Using a scaled modulus, Equation 7 can be expressed as

$$\begin{aligned} \boldsymbol{\sigma}'_{t+\Delta t} &= \boldsymbol{\sigma}'_t + 2\mu^*\,\boldsymbol{d}'\,\Delta t\; - 2\mu^*\,\dot{\bar{\varepsilon}}\,\Delta t\,\frac{3}{2}\frac{\boldsymbol{\sigma}'_t}{\sigma_t^{vm}} \\ &= \boldsymbol{\sigma}^T - 3\mu^*\,\dot{\bar{\varepsilon}}\,\Delta t\,\frac{\boldsymbol{\sigma}'_t}{\sigma_t^{vm}}, \end{aligned} \tag{10}$$

where $\mu^* = \mu\mathcal{M}$ and $\boldsymbol{\sigma}^T$ is defined as the trial stress. The trial stress is the stress that would result if there were no plastic deformation within the increment. Equation 10 is identical to the classical forward-difference integration over a time step, but with a reduced shear modulus.

2.1.5 Solution Method

The plastic strain rate is determined by satisfying the yield function, ϕ, which relates the material strength at the end of the time step, $\bar{\sigma}(\bar{\varepsilon}, \dot{\bar{\varepsilon}}, T, p, \ldots)$, to the stress state. For J2-flow theory, the tensor stress state is captured by the scalar von Mises stress, resulting in

$$\phi = \bar{\sigma}(\bar{\varepsilon}, \dot{\bar{\varepsilon}}, T, p, \ldots) - \sigma_{t+\Delta t}^{vm} = 0\,. \tag{11}$$

For simple material strength models, Equation 11 is a function of a single unknown plastic strain rate. Solution proceeds by multiplying both sides of Equation 10 by itself and then by 3/2.

$$\begin{aligned} (\sigma_{t+\Delta t}^{vm})^2 &= \frac{3}{2}\boldsymbol{\sigma}'_{t+\Delta t}\!:\boldsymbol{\sigma}'_{t+\Delta t} \\ &= \frac{3}{2}\boldsymbol{\sigma}^T\!:\boldsymbol{\sigma}^T - 2(3\mu^*\dot{\bar{\varepsilon}}\,\Delta t)\,\frac{3}{2}\frac{\boldsymbol{\sigma}'_t\!:\boldsymbol{\sigma}^T}{\sigma_t^{vm}} + (3\mu^*\dot{\bar{\varepsilon}}\,\Delta t)^2\,\frac{3}{2}\frac{\boldsymbol{\sigma}'_t\!:\boldsymbol{\sigma}'_t}{(\sigma_t^{vm})^2}\,. \end{aligned} \tag{12}$$

Tensor inner products are represented as an effective trial stress, σ_{eff}^{T}, and an auxiliary stress, σ_{Aux}. The inner product in the last term is the von Mises stress at the beginning of the time step. The resulting expression used in the yield function, Equation 11 is

$$\sigma_{t+\Delta t}^{vm} = \sqrt{\left(\sigma_{\text{eff}}^{T}\right)^2 - 2(3\mu^* \dot{\bar{\varepsilon}}\,\Delta t)\,\sigma_{\text{Aux}} + (3\mu^* \dot{\bar{\varepsilon}}\,\Delta t)^2}\,. \tag{13}$$

Everything is known in Equation 13 except the plastic strain rate. The yield function from Equation 11 is solved iteratively for the plastic strain rate using the RT-Safe algorithm from Numerical Recipes (Press et al. 1992). It is a Newton–Raphson iteration algorithm combined with bisection that provides ever-tightening bounds to limit solution excursions.

The method and the reduced modulus from Equation 10 apply only for continuing plastic deformation. If the prior stress state is elastic, the standard radial return solution is used. Otherwise, the time step would need to split into elastic and plastic portions. This is possible, but likely not worth the additional expense. Also, if the angle between the yield surface normal and the strain increment determined by the inner product is greater than 85°, the radial return solution is used. This condition traps unloading or reverse loading over a single time step. Reverse loading violates the assumption of continued plastic flow.

2.2 Algorithm Verification

2.2.1 Nonproportional Loading with J2-Flow Theory

Nonproportional loading simulations are presented to demonstrate the robustness of the method and to compare its accuracy with a standard radial return solution. The shear modulus is taken as 33.33 GPa and the yield strength is 500 MPa so that the effective strain at yield is 0.005. The bulk modulus is 80 GPa but, since the deformations are nominally isochoric, the pressures are inconsequential. The first simulation has a smoothly varying loading direction, and it has a zero hardening modulus. The second simulation has a discontinuous path change and a hardening rate of 1186 MPa.

The nonhardening simulation has a smoothly varying strain rate specified by

$$\begin{aligned} \dot{\varepsilon}_{xx}\,(\text{ms}^{-1}) &= 0.05\cos(t) \\ \dot{\varepsilon}_{yy}\,(\text{ms}^{-1}) &= -0.05\cos(t+\pi/3)\,. \\ \dot{\varepsilon}_{zz}\,(\text{ms}^{-1}) &= -0.05\cos(t-\pi/3) \end{aligned} \tag{14}$$

A time increment of 0.0005 ms ($\Delta\varepsilon = 25\text{x}10^{-6}$) is run for 8 ms to establish a converged baseline. With this time increment, the radial return solution and the reduced-modulus solution differed after the fourth significant digit. Additional simulations were run with large constant time increments of 0.5 ms ($\Delta\varepsilon = 0.025$) and 1.5 ms ($\Delta\varepsilon = 0.075$) to compare with the baseline.

These results are shown in Figure 3, where the solid line is the baseline solution for σ_{xx}. Since the initial strain increment is multiples of the initial yield strain, the raw plots show a systematic shift with time step. To adjust for this, the strain is shifted lower in the plots. The shift is calculated by subtracting the 0.005 yield strain from the initial strain increment and then dividing by 2 to center the strain in the increment. This gives shifts of 0.010 and 0.035 for the 0.5- and 1.5-ms time increments, respectively. The results show that the reduced-modulus solution is slightly closer to the baseline than the radial return and the method is robust at strain increments 15 times the yield strain.

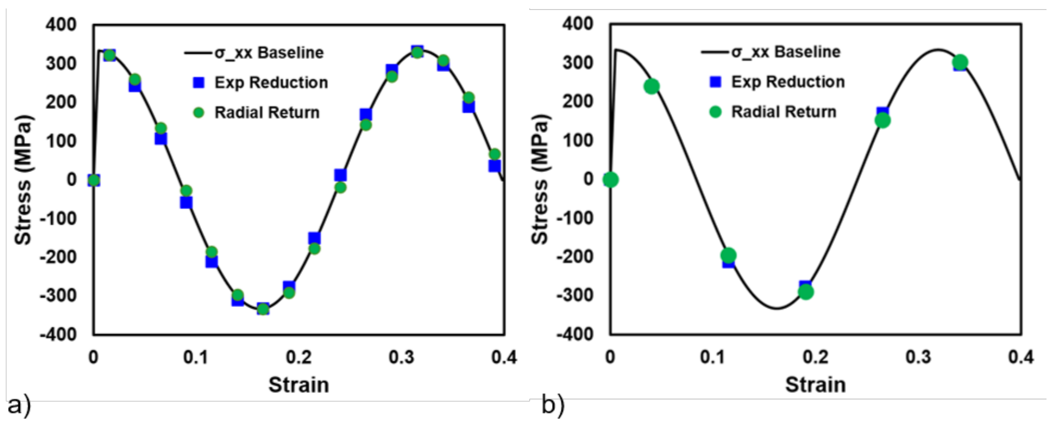

Figure 3. **x-direction stress resulting from the nonproportional loading described by Equation 14 for radial return and the reduced-modulus method. Solid lines represent the converged solution with 20 × 10^{-6} strain increments. Symbols represent the solutions for strain increments of a) 0.025 and b) 0.075.**

2.2.2 Evaluation with Abrupt Path Change

The second example has a discontinuous path change. The loading is isochoric extension along the y-axis at a strain rate of 0.0125 ms^{-1} for 3.2 ms followed by simple shear in the x-direction at a shear rate of 0.0125 ms^{-1}. The baseline solution is calculated at a time step of 0.0005 ms ($\Delta\varepsilon = 6.25\text{x}10^{-6}$). The evaluation is performed with a time step of 0.8 ms ($\Delta\varepsilon = 0.01$), where the strain increment is twice the yield strain. The results are provided in Figure 4. The solid line is the baseline solution and the discrete symbols are for the 0.8-ms time step. Figure 4a shows the decay of the y-direction deviatoric stress, σ_{yy}, and Figure 4b shows the shear stress increase, τ_{xy}. The modulus reduction algorithm matches the baseline decay slightly better than the radial return and handles the abrupt transition well.

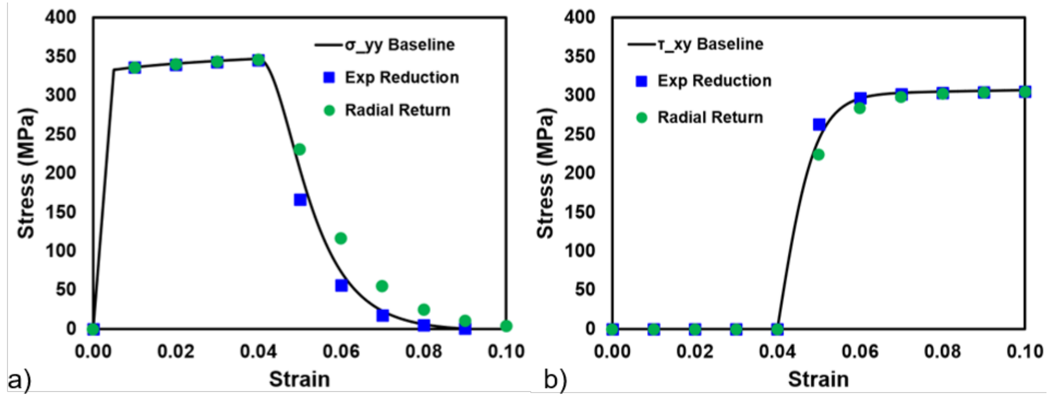

Figure 4. Integration algorithm evaluated for an abrupt path change from uniaxial extension along the y-axis to simple shear in the x-direction. a) y-direction and b) shear stress.

The shear stress results are shown in Figure 4b. While both methods miss the converged solution by approximately the same amount on the first time step after the loading path change, the modulus reduction technique matches the baseline result on subsequent time steps. It takes the radial return a few time steps to saturate to the proper value.

2.3 Application to a Corner Theory

2.3.1 Corner Theory Model

The intent of the reduced-modulus approach is to provide an alternative integration technique for other yield functions where the plastic return for large strain increments is difficult to handle numerically. Based on a generalization of Equation 10, it is proposed that the deviatoric stress can be integrated over a time step by

$$\boldsymbol{\sigma}'_{t+\Delta t} = \boldsymbol{\sigma}^T - 3\mu^* \, \dot{\bar{\varepsilon}} \, \Delta t \sqrt{\frac{2}{3}} \frac{\boldsymbol{P}}{\|\boldsymbol{P}\|} , \tag{15}$$

where $\boldsymbol{P}$ is a tensor in the direction of plastic flow.

The specific example chosen for illustration is Simo's (1987) inclusion of a corner effect on a J2-flow theory surface. Details of the model and the particular corner function are provided in Simo (1987) and Kuroda and Tvergaard (2001a). Only the essential elements are provided here.

A corner theory model mimics a vertex on the yield surface, as is suggested by experiments and crystal plasticity simulations (e.g., Hecker 1976; Kuwabara et al. 2000; Bassani and Racheria 2011). A corner on a yield surface has a nonunique normal. Hence, plastic flow can occur in a multitude of directions for a given stress state. This freedom can facilitate prediction of strain localization. An additional feature is that the stress state need not be modified significantly to accommodate the plastic deformation. In corner theory models, the unrestrained plastic flow direction is confined to a cone of directions constructed at the vertex. The plastic flow direction outside of the cone gradually returns to the normality flow rule (Figure 5).

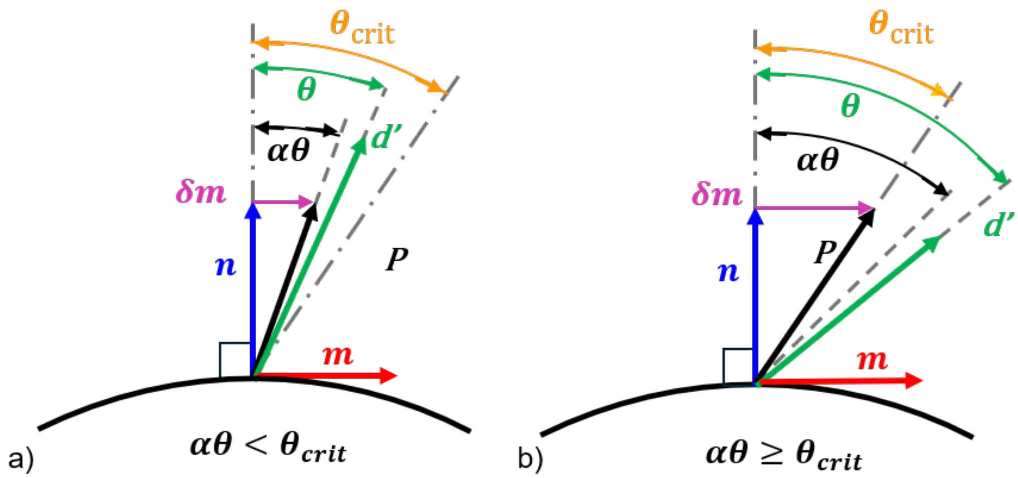

Figure 5. Illustration of plastic return direction for the corner theory model for loading a) within the cone defined by the critical angle and b) outside of the cone. Adapted from Kuroda and Tvergaard (2001a).

In the Simo model (1987), the plastic flow direction, $\boldsymbol{P}$, is specified as a linear combination of the normal to the yield surface, $\boldsymbol{n}$, and a direction, $\boldsymbol{m}$, orthogonal to the normal in the direction of the applied deviatoric strain rate. The plastic flow direction is given by

$$\boldsymbol{P} = \boldsymbol{n} + \delta\,\boldsymbol{m}\,. \tag{16}$$

The direction orthogonal to the normal is determined by

$$\boldsymbol{m} = \frac{\boldsymbol{d}' - \boldsymbol{n}\,(\boldsymbol{n}\!:\!\boldsymbol{d}')}{\|\boldsymbol{d}' - \boldsymbol{n}\,(\boldsymbol{n}\!:\!\boldsymbol{d}')\|}\,. \tag{17}$$

For an underlying J2-flow surface, the unit normal calculated at the beginning of the time increment is

$$\boldsymbol{n} = \sqrt{\frac{3}{2}}\,\frac{\boldsymbol{\sigma}_t'}{\sigma_t^{vm}}\,. \tag{18}$$

The parameter δ in Equation 16 controls the deviation of the plastic flow direction from the normal. It is a function of the angle of the applied strain increment from the normal. The angle the applied strain rate deviates from the yield surface normal is determined by standard inner product relations:

$$\theta = \cos^{-1}\left(\frac{\boldsymbol{n}:\boldsymbol{d}'}{\|\boldsymbol{d}'\|}\right) . \tag{19}$$

Following Kuroda and Tvergaard (2001a), δ in Equation 16 is given by

$$\delta = \begin{cases} \tan(\alpha\,\theta) & \text{for} \quad \alpha\,\theta < \theta_{\text{crit}} \\ \tan(\theta_{\text{crit}}) & \text{for} \quad \alpha\,\theta \geq \theta_{\text{crit}} \, , \end{cases} \tag{20}$$

where θ_{crit} is the critical angle beyond which the corner effect begins to be reduced.

The constant α in Equation 20 is a function of the strength and shear modulus:

$$\alpha = \frac{1}{1 + c\ \bar{\sigma}/\mu} . \tag{21}$$

The order-one constant c regulates the flow stress dependence of c. For $c = 0$ ($\alpha = 1$), the plastic return direction, $\boldsymbol{P}$, is coaxial with the applied strain increment for angles less than θ_{crit}. As c increases and α decreases, less of the orthogonal component is added to the normal, which moves the plastic flow direction a bit closer to the surface normal. The intent of the factor is to account for material viscosity (Kuroda and Tvergaard 2001a), but it also weakens the effect of the vertex, which allows the stress state to migrate slowly along the yield surface. This is important for simulations tracking deformation to large strain and beyond initiation of localization.

2.3.2 Corner Theory Implementation

Implementation parallels the J2-flow theory example of Equation 12. Equation 15 is contracted with itself and multiplied by 3/2.

$$(\sigma^{vm}_{t+\Delta t})^2 = \frac{3}{2}\boldsymbol{\sigma}^T:\boldsymbol{\sigma}^T - 2(3\mu^*\dot{\bar{\varepsilon}}\,\Delta t)\sqrt{\tfrac{2}{3}}\frac{\boldsymbol{P}:\boldsymbol{\sigma}^T}{\|\boldsymbol{P}\|} + (3\mu^*\dot{\bar{\varepsilon}}\,\Delta t)^2\frac{\boldsymbol{P}:\boldsymbol{P}}{\|\boldsymbol{P}\|^2} . \tag{22}$$

This provides an expression for the von Mises stress at the end of the time increment similar to Equation 13, but with a different calculation for $\hat{\sigma}_{\text{Aux}}$.

$$\sigma^{vm}_{t+\Delta t} = \sqrt{\left(\sigma^T_{\text{eff}}\right)^2 - 2(3\mu^*\dot{\bar{\varepsilon}}\,\Delta t)\,\hat{\sigma}_{\text{Aux}} + (3\mu^*\dot{\bar{\varepsilon}}\,\Delta t)^2} . \tag{23}$$

When coupled with the J2-flow theory yield criterion from Equation 11, the solution for the plastic strain rate proceeds the same as the J2-flow model by using the RT-Safe algorithm. With the strain rate calculated, the stress is computed from Equation 15.

2.3.3 Corner Theory Behavior

The behavior of the corner theory model is illustrated through the same nonproportional loading examples used to verify the integration algorithm for J2-flow theory. The material properties and boundary conditions are unchanged. The only difference is the yield surface type. The cone angles were taken as 20° and 50°, with $c = 3$.

Results from the simulation with the cosine-based, nonproportional loading of Equation 14 are shown in Figure 6. The calculations were run with strain increments of $\Delta\varepsilon = 25\text{x}10^{-6}$ and $\Delta\varepsilon = 0.025$, shown by the dashed lines and symbols, respectively. The curves are shifted based on the initial strain increment as they are in Figure 3. The results show that the stress remains constant initially, and then it follows the baseline J2-flow theory trajectory with a phase lag. The phase lag is indicative of the deformation prior to the corner being dragged along the yield surface. The larger the cone angle, the greater the stress deviation before the vertex begins migrating.

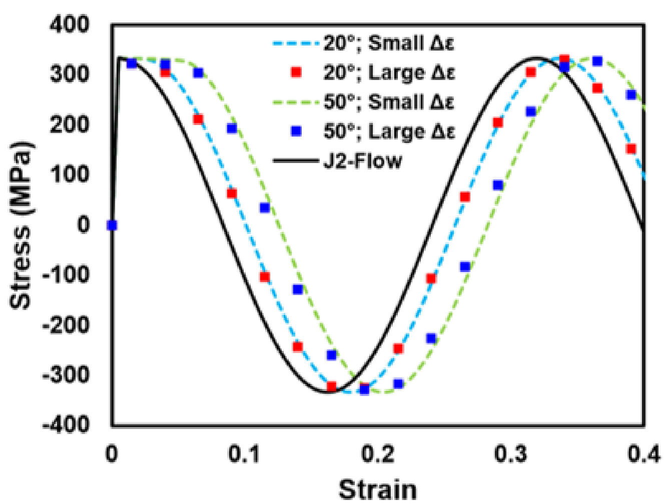

Figure 6. Corner theory model results for the nonproportional loading given in Equation 14 compared with the J2-flow theory solution. The larger critical angle results in a greater lag between the applied loading and the following stress. The solid and dashed lines are for strain increments of 25×10^{-6} and symbols are for strain increments of 0.025.

Results for the discontinuous path change calculations are presented along with the J2-flow theory stress in Figure 7. The data show the influence of the c parameter in addition to the effect of the cone angle. The dashed cyan line is the corner response for a 20° vertex angle and $c = 3$ with a strain increment of 6.25×10^{-6}. The symbols are results with strain increments of 0.005, which is the yield strain. The initial extension stress is the same for all simulations because the loading is proportional. The angle of the abrupt path change is greater than critical cone angle. This forces the stress to change immediately, and the vertex begins migrating around the yield surface.

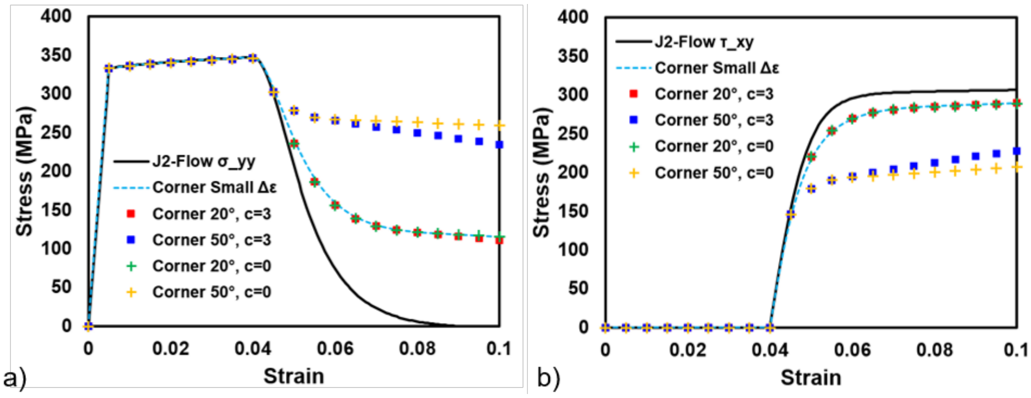

Figure 7. Corner theory simulation results for the discontinuous path change. a) y-direction and b) shear stresses. The black solid and dashed cyan line are for strain increments of 6.25×10^{-6} and symbols correspond to strain increments of 0.005.

The vertex migration nearly ceases when the angle between the stress tensor and the applied deformation falls within the critical angle. This is demonstrated by the stress change in Figure 7a being substantially less for the 50° vertex angle than the 20° vertex angle. Consistent with this, the shear stress in Figure 7b evolves further for the 20° vertex angle than for the 50° vertex angle. The reduced shear stress for the corner model would permit easier shear deformation than the J2-flow model, potentially facilitating shear strain localization.

The stress evolution for loading within the vertex cone is also influenced by c. Higher c values point the plastic return direction closer to the yield surface normal, which causes the stress to migrate faster. For a nonhardening material, a value of $c = 0$ should prohibit stress evolution for loadings within the vertex cone. Strain hardening reduces the distance of the plastic return, causing a change in stress even for $c = 0$.

2.4 Tresca Yield Criterion

The Tresca yield criterion is long-established function with a reduced flow strength in plane strain and yield surface vertices that may be beneficial for strain localization and fracture predictions. The Tresca criterion is based on the maximum shear stress, which is evaluated as the difference between the maximum and minimum principal stresses. This creates a faceted yield surface with natural vertices at the intersection of the facets.

2.4.1 Difficulties with Associated-Flow Tresca Criterion

For corner theories or for yield surface vertices resulting from crystal plasticity, the vertices are associated with prior loading or tied to the material microstructure. The vertices for the Tresca yield surface are different in nature as they are associated with stress states. They exist where two of the principal stresses are equal. If the principal stresses are ordered, only two principal stress states are permitted at the vertices:

$$\left\{\frac{2}{3}\sigma^{vm}, \frac{-1}{3}\sigma^{vm}, \frac{-1}{3}\sigma^{vm}\right\} \quad \text{or} \quad \left\{\frac{1}{3}\sigma^{vm}, \frac{1}{3}\sigma^{vm}, \frac{-2}{3}\sigma^{vm}\right\}. \tag{24}$$

The first is associated with extension and the other compression. This vertex condition creates an unusual and very restrictive set of constraints on the stress state.

If using an associated flow rule with a Tresca yield surface, stress states not on a vertex create plane-strain plastic flow where one of the principal plastic strain rates is zero. If the overall deformation is not plane strain, stress builds in this zero-flow direction. The stress state eventually evolves to a vertex state where general plastic flow can occur. At the vertex, however, two of the principal stress must be the same, which places unrealistic constraints on the stress state. Having severe restrictions on either the stress state or the plastic strain increment direction makes a Tresca yield criterion with an associated flow rule model unappealing.

2.4.2 Nonassociated-Flow Tresca Criterion

Nonassociated flow models use different functions for the yield surface and plastic flow potential. Hill's (1950) classical plasticity book maintains the distinction between the yield surface and flow rule, and multiple studies (e.g., Raniecki and Bruhns 1981; Bassani and Racheria 2011) demonstrate that nonassociated flow models can lead to flow-field bifurcation at lower strain levels than associated flow models. In addition, results from crystal plasticity models suggest different yield surfaces and flow potentials (e.g., Bassani and Racherla 2011; Kuroda and Tvergaard 2001b).

Although there is motivation for nonassociated models, they are uncommon in practice. The reason is mostly because of practicality rather than physical correctness. Yield surfaces are difficult to determine, and plastic flow potentials are even more difficult to characterize. The complexity and data requirements are prohibitive.

A simple nonassociated model is chosen to provide the differential between the normal and shear stresses of the Tresca yield criterion without the unphysical constraints of the associated flow model. A J2-flow plastic potential surface is used with the Tresca yield surface. This approach is also used in EPIC (Beissel and Gerlach 2025).

2.4.2.1 Flow Rule

The starting point for the radial return solution for the J2-flow potential is a backward-difference incremental equation for the stress. This is similar to Equation 10 but plastic return direction is coaxial with the stress at the end of the time increment:

$$\boldsymbol{\sigma}'_{t+\Delta t} = \boldsymbol{\sigma}^T - 3\mu\,\dot{\bar{\varepsilon}}\,\Delta t\,\frac{\boldsymbol{\sigma}'_{t+\Delta t}}{\sigma^{vm}_{t+\Delta t}}\,. \tag{25}$$

With minor rearrangement, the backward-difference form aligns the Cauchy stress tensor at the end of the time increment with the trial stress:

$$\boldsymbol{\sigma}'_{t+\Delta t}\left(1 + \frac{3\mu\,\dot{\bar{\varepsilon}}\,\Delta t}{\sigma^{vm}_{t+\Delta t}}\right) = \boldsymbol{\sigma}^T\,. \tag{26}$$

Because the stress at the end of the time increment is coaxial with the trial stress, the effective stress and principal stresses (σ_{p1}, σ_{p2} and σ_{p3}) are similarly related. Consequently, the following hold:

$$\sigma^{vm}_{t+\Delta t}\left(1 + \frac{3\mu\,\dot{\bar{\varepsilon}}\,\Delta t}{\sigma^{vm}_{t+\Delta t}}\right) = \sigma^T_{\text{eff}}\,, \tag{27}$$

and

$$\left(\sigma_{p1} - \sigma_{p3}\right)\left(1 + \frac{3\mu\,\dot{\bar{\varepsilon}}\,\Delta t}{\sigma^{vm}_{t+\Delta t}}\right) = \left(\sigma^T_{p1} - \sigma^T_{p3}\right). \tag{28}$$

Dividing Equation 28 by Equation 27 provides a relation with the strain rate eliminated.

$$\frac{\left(\sigma_{p1} - \sigma_{p3}\right)}{\sigma^{vm}_{t+\Delta t}} = \frac{\left(\sigma^T_{p1} - \sigma^T_{p3}\right)}{\sigma^T_{\text{eff}}}\,. \tag{29}$$

Equation 28 can be rewritten to give the return stress mapping as

$$\left(\sigma_{p1} - \sigma_{p3}\right) = \left(\sigma^T_{p1} - \sigma^T_{p3}\right) - 3\mu\,\dot{\bar{\varepsilon}}\,\Delta t\,\frac{\left(\sigma_{p1} - \sigma_{p3}\right)}{\sigma^{vm}_{t+\Delta t}}\,. \tag{30}$$

2.4.2.2 Yield Function

If the principal stresses are ordered largest to smallest, the Tresca yield function is

$$\phi = \bar{\sigma}(\bar{\varepsilon}, \dot{\bar{\varepsilon}}, T, p, \ldots) - \left(\sigma_{p1} - \sigma_{p3}\right) = 0\,. \tag{31}$$

Substituting from Equation 30 and using Equation 29, the yield function becomes

$$\phi = \bar{\sigma}(\bar{\varepsilon}, \dot{\bar{\varepsilon}}, T, p, \dots) - \left[\left(\sigma_{p1}^{T} - \sigma_{p3}^{T} \right) - 3\mu\, \dot{\bar{\varepsilon}}\, \Delta t\, \frac{\left(\sigma_{p1}^{T} - \sigma_{p3}^{T} \right)}{\sigma_{\text{eff}}^{T}} \right] = 0\,. \qquad (32)$$

This yield function can be solved iteratively for the plastic strain rate using the RT-Safe algorithm applied previously to the J2-flow and corner theory solutions. Since the return mapping algorithm for the Tresca model is backward difference and radial return, the algorithm is very robust at any strain increment. The exponential modulus reduction is not needed.

2.4.3 Behavior with the Tresca Yield Criterion

The results from the Tresca yield surface for the discontinuous path change are shown in Figure 8. The initial isochoric extension follows the J2-flow theory solution because the proportional deformation aligns with a yield surface vertex state. The y-direction stress deviates somewhat from the J2-flow solution after the path change because the plastic strain direction is projected back from the difference of the principal trial stress rather than the effective trail stress.

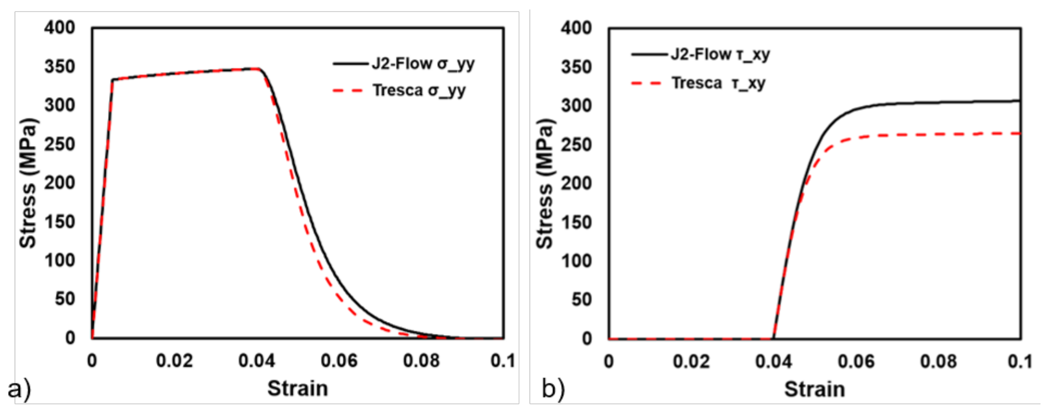

Figure 8. Tresca model results for the discontinuous strain path. a) Extension stress along the y-direction and b) shear stress.

The shear response following the path change differs substantially from the J2-flow result because it lies on a facet of the Tresca yield surface. The shear stress required for plastic flow is $\sqrt{3}\,/\,2$ that of the J2-flow result. The reduced stress corresponds to lower energy dissipation in shear compared with the J2-flow theory model.

The nonproportional cosine loading of Equation 14 illustrates the faceted nature of the Tresca yield surface in Figure 9. The solution roughly follows the J2-flow result but with nearly linear segments rather than a smooth cosine curve. The six vertices of the Tresca yield surface correspond to the vertices in the red-dashed curve and the connecting segments correspond to the facets.

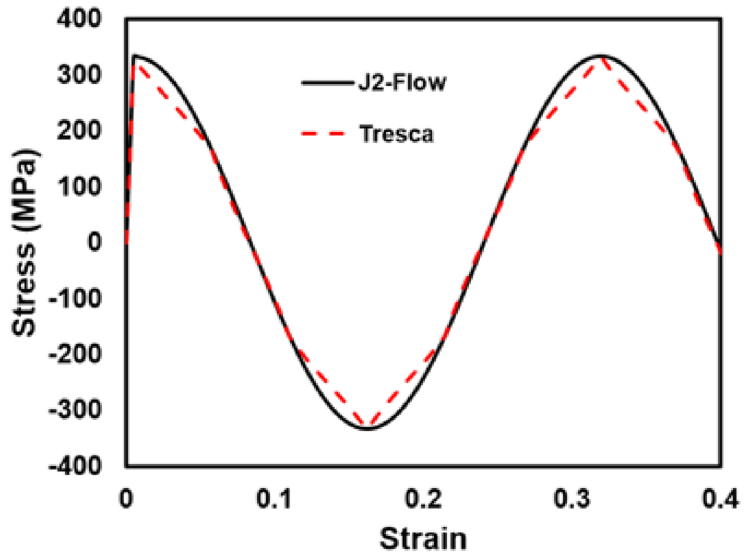

Figure 9. Stress in the x-direction for the J2-flow and Tresca yield surfaces with the nonproportional loading defined by Equation 14. The stress history for the Tresca yield surface is faceted with vertices corresponding to the yield surface vertices.

As with the shear in the discontinuous loading simulations, the stress is always lower for the Tresca material, so the energy expended during deformation will be lower for the Tresca model.

2.5 Analytic EOS

An EOS is needed for a constitutive model usable in a numerical simulation. The form employed here is a modification of the EOS proposed by Hayes (Sheffield et al. 1976). The isothermal component is the Murnaghan EOS (Murnaghan 1944). The thermal component has been modified from Hayes's function to satisfy the definition of the Grüneisen parameter in Equation 39, below.

This EOS is suitable for static or shock loading. However, since the bulk modulus does not soften with temperature, the reference bulk modulus may need adjustment if this dependency is important in high-temperature static loadings.

2.5.1 Thermodynamic Relations

2.5.1.1 Helmholtz Energy, Internal Energy, and Entropy

The EOS used in the simulations is based on a Helmholtz-specific energy function:

$$\mathcal{F}(v,T) = \mathrm{F}(v) + c_v\left[(T - T_0)\left(1 - \Gamma \ln\left(\frac{v}{v_0}\right)\right) - T \ln\left(\frac{T}{T_0}\right)\right] \tag{33}$$

where v is the specific volume, c_v is the specific heat, T is the temperature, and Γ is the Grüneisen constant. The zero subscript denotes a reference value, typically taken at ambient conditions. The athermal contribution, $\mathrm{F}(v)$, follows the Murnaghan form:

$$\mathrm{F}(v) = \frac{K\,v_0}{k'(k'-1)}\left[\left(\frac{v}{v_0}\right)^{1-k'} - 1 - (k'-1)\left(1-\frac{v}{v_0}\right)\right]. \tag{34}$$

Here, K is the reference bulk modulus and $k'$is the derivative of the bulk modulus with respect to pressure.

It is often more convenient to use relative volumes rather than specific volume in hydrocodes since the specific volume often appears normalized by its reference value. This is defined as

$$V = \frac{v}{v_0} = \frac{\rho_0}{\rho}. \tag{35}$$

It is also often more convenient to work with energy per unit reference volume rather than specific energy to avoid density factors when integrating the strain work. The Helmholtz energy per reference volume expressed as a function of the relative volume is

$$\tilde{\mathcal{F}}(V,T) = \tilde{\mathrm{F}}(V) + \rho_0 c_v\left[(T-T_0)(1-\Gamma\ln(V)) - T\ln\left(\frac{T}{T_0}\right)\right] \tag{36}$$

with

$$\tilde{\mathrm{F}}(V) = \frac{K}{k'(k'-1)}\left[(V)^{1-k'} - 1 - (k'-1)(1-V)\right]. \tag{37}$$

2.5.1.2 Entropy and Internal Energy

Following traditional thermodynamics, the entropy per unit reference volume is determined as

$$\tilde{\mathcal{S}} = -\frac{d\,\tilde{\mathcal{F}}(V,T)}{d\,T} = \rho_0 c_v\left[\Gamma\ln(V) + \ln\left(\frac{T}{T_0}\right)\right]. \tag{38}$$

This form satisfies the definition of the definition of the Grüneisen parameter at constant entropy:

$$\Gamma = -\left.\frac{d\ln T}{d\ln V}\right)_{\mathcal{S}}. \tag{39}$$

The internal energy per unit reference volume is determined from the Helmholtz energy and the entropy by

$$\tilde{\mathcal{U}}(V, \tilde{\mathcal{S}}) = \tilde{\mathcal{F}}(V, T) + T\tilde{\mathcal{S}} \,. \tag{40}$$

This becomes

$$\begin{aligned} \tilde{\mathcal{U}}(V, \tilde{\mathcal{S}}) &= \tilde{\mathrm{F}}(V) + \rho_0 c_v [T - T_0(1 - \Gamma \ln(V))] \\ &= \tilde{\mathrm{F}}(V) + \rho_0 c_v (T - T_0) + \rho_0 c_v T_0 \Gamma \ln(V) \,. \end{aligned} \tag{41}$$

2.5.1.3 Temperature and Pressure

The temperature can then be determined from the internal energy and relative volume by rearranging Equation 41.

$$T = \frac{\tilde{\mathcal{U}}(V, \tilde{\mathcal{S}}) - \tilde{\mathrm{F}}(V)}{\rho_0 c_v} + T_0(1 - \Gamma \ln(V)) \,. \tag{42}$$

The explicit dependence of the internal energy on entropy is a reminder that temperature changes from dissipative processes are captured by internal energy. Temperature can also change with relative volume at constant entropy, as indicated by the entropy equation.

The pressure is determined from the Helmholtz energy as

$$p = -\frac{d\,\tilde{\mathcal{F}}(V, T)}{d\,V} = -\tilde{\mathrm{F}}'(V) + \rho_0 c_v (T - T_0)\frac{\Gamma}{V} \,, \tag{43}$$

where the derivative of the Murnaghan function is

$$\tilde{\mathrm{F}}'(V) = -\frac{K}{k'}\left[(V)^{-k'} - 1\right]. \tag{44}$$

Replacing the temperature dependence by a function of the internal energy, the pressure becomes

$$p = -\tilde{\mathrm{F}}'(V) - \frac{\Gamma}{V}\tilde{\mathrm{F}}(V) - \frac{\Gamma}{V}\rho_0 c_v T_0 \Gamma \ln(V) + \frac{\Gamma}{V}\,\tilde{\mathcal{U}} \,. \tag{45}$$

This resembles the Grüneisen EOS form where the pressure is determined from the sum of volume-dependent terms and a term with the internal energy.

2.5.2 Comparison with Mie–Grüneisen

The Mie–Grüneisen form of the EOS with a linear dependence of the shock velocity on the particle velocity is

$$p = \frac{\rho_o C_0^2 \eta \left[1 + \left(1 - \frac{\Gamma}{2}\right)\eta\right]}{[1 - (1 - S_1)\eta]^2} + \frac{\Gamma}{V}\,\tilde{\mathcal{U}} \,, \tag{46}$$

where C_0 is the reference longitudinal sound speed, $S_1$is the slope of the sound velocity-particle velocity curve, and η is the compression, defined as

$$\eta = \frac{1}{V} - 1\,. \tag{47}$$

The modified Hayes version and the Mie–Grüneisen can be compared by identifying the bulk modulus as $K = \rho_o C_0^2$ and the derivative of the bulk modulus with respect to pressure as $k' = 4\,S_1 - 1$. A comparison of the volume-dependent terms is plotted as a function of compression in Figure 10 for the generic steel and aluminum properties given in Table 1. Although the functional forms are very different, the curves are in good agreement for compressions below 0.4.

Table 1. Properties used in comparison of the Murnaghan form with the Mie–Grüneisen form.

	ρ_0 (g/mm³)	K (MPa)	S_1	Γ	c_v(mJ/g-K)	k'
Steel	0.0078	140,000	1.49	1.67	475	4.96
Aluminum	0.0027	760,000	1.4	2.0	924	4.6

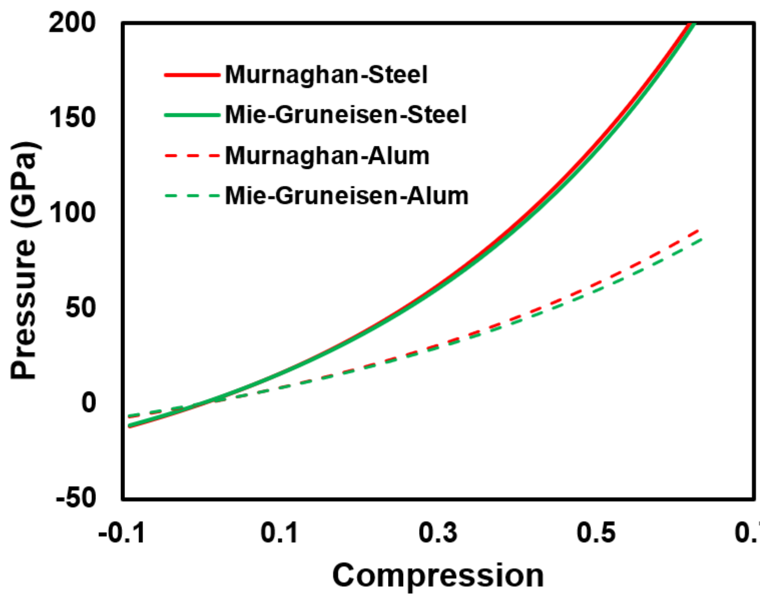

Figure 10. Volume dependence of the pressure for the Hayes and Mie–Grüneisen EOS forms using properties from Table 1.

3. Sample Application

3.1 Model Description

A sample application illustrating the behavior of the yield surfaces is a right rectangular cylinder impacting a circular plate. The steel cylinder is 25 mm long and 20 mm in diameter. It impacts a 152-mm-diameter aluminum plate, 38.1 mm thick, at 850 m/s. The axisymmetric finite element mesh has three elements per millimeter in both the radial and axial directions. The simulation is run with quad elements in ALE3D (Dawson et al. 2020) in Arbitrary Lagrangian–Eulerian mode using equipotential relaxation on the mesh.

The steel was modeled using the Steinberg–Guinan form with a yield strength of 2.2 GPa, a hardening coefficient of 2, and a hardening exponent of 0.5. The strength was capped at 2.5 GPa. The aluminum was modeled with the yield functions described in the previous sections. For the corner theory model, the critical angle was 20° and $c = 3$. The flow strength used a rate and temperature independent Johnson–Cook model:

$$\bar{\sigma}\ (\text{MPa}) = 250 + 300\ \bar{\varepsilon}^{0.25}\ , \tag{48}$$

with a strength cap of 300 MPa. Thermal softening was purposefully omitted to highlight the effect of the yield surface and plastic flow rules. The failure strain for the Johnson–Cook failure model for the aluminum was represented by

$$\varepsilon_f = \left[0.095 + 1.464 \exp\left(\frac{1.15\, p}{\bar{\sigma}}\right)\right] \left[1 - 0.006 \ln\left(\frac{\dot{\bar{\varepsilon}}}{1}\right)\right] \left[1 - 0.345\left(\frac{T - 298}{875 - 298}\right)\right]\ , \tag{49}$$

with a minimum failure strain of 0.062. These were motivated by parameters for 7085 aluminum but the failure strain was reduced.

3.2 Predicted Velocity Fields

Predicted velocity fields are shown in Figure 11 for the J2-flow, corner, and Tresca yield surfaces. At 60 μs, presented in the upper portion of Figure 11, the velocity fields are similar in both form and magnitude. A cone of material is moving nearly rigidly ahead of the penetrator. The velocity field smoothly transitions to zero velocity remote from the penetrator. The velocity fields are also similar at times prior to 60 μs. Cavity expansion dominates the energy dissipation at early times, and the differences among these yield functions are not prominent for cavity expansion. At 60 μs, the projectile is moving fastest in the Tresca material and slowest in the J2-flow material.

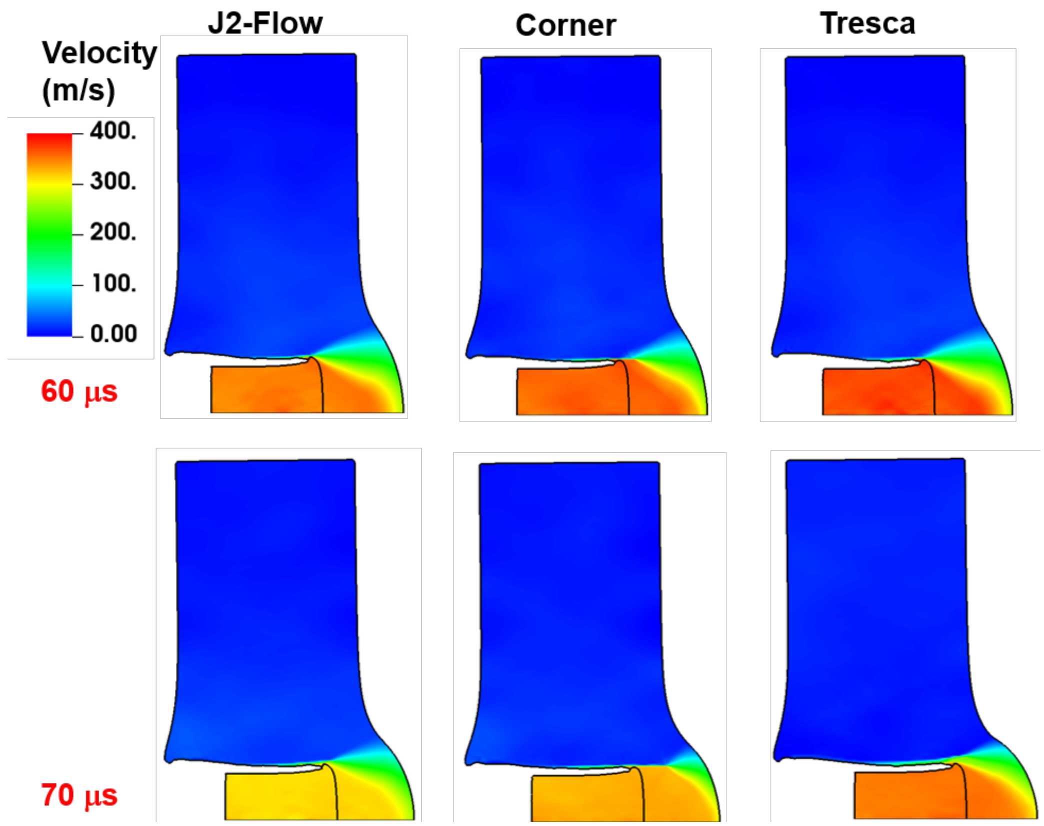

Figure 11. Predicted velocity fields for the J2-flow, corner, and Tresca yield surface models at 60 and 70 μs. The velocity scale applies to both sets of plots.

Notable differences are emerging at 70 μs. The bottom row of Figure 11 reveals penetrator velocity differences as well as differences in the form of the transition velocity field. In particular, the corner theory result in the center column has developed a velocity discontinuity extending from the penetrator interface to approximately halfway to the right-hand free surface. The fan of velocities emanates from the tip of the discontinuity, substantially changing the remainder of the deformation field compared with the J2-flow and Tresca solutions. The strength model used in these simulations has no temperature dependence, so the differences can be attributed solely to yield surface shape without compounding effects of thermal softening.

By 80 μs, the velocity discontinuity in the corner theory simulation has nearly reached the free surface (Figure 12). A clean plug is forming and there is only a small velocity decrease to the plot at 90 μs. The shear fracture allows the projectile velocity for the corner theory model to exceed that of the Tresca model at 80 μs. The velocity fields for the J2-flow and Tresca solutions have similar extent at 80 μs, but the velocity is lower for the J2-flow calculation. The Tresca yield surface has a lower stress in shear, so less energy is dissipated to slow the projectile. The yield surface difference is also affecting the form of the velocity field by 90 μs. The velocity fan is persisting for the Tresca simulation, while the J2-flow result is becoming more slug-like.

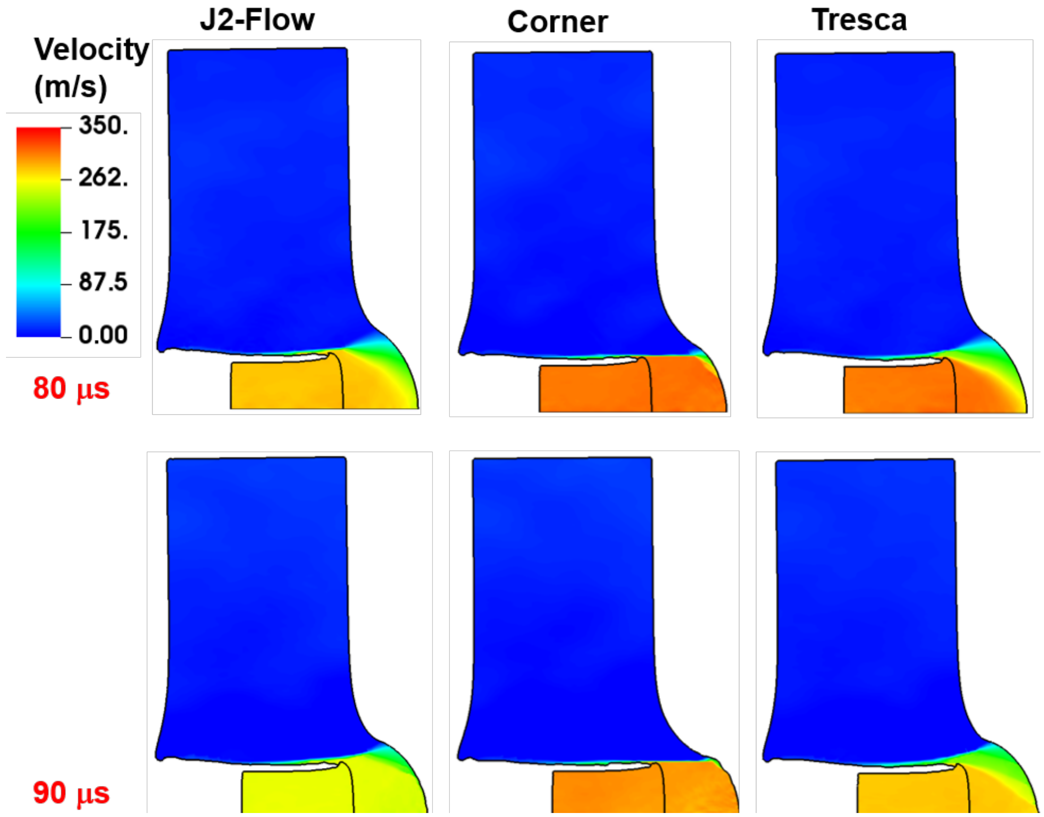

Figure 12. Predicted velocity fields for the J2-flow, corner, and Tresca yield surface models at 80 and 90 μs. The velocity scale applies to both sets of plots.

The strain has localized and velocity discontinuities are evident for all three yield functions by 100 μs (Figure 13). The corner theory simulation has formed a cylindrical plug while the J2-flow and Tresca models create a plug with a flare at the free surface end. The location of the concentrated shear for these late-forming localizations is modulated by the shortest path from the projectile corner to the free surface. Strain would prefer to localize where the remaining ligament is the smallest.

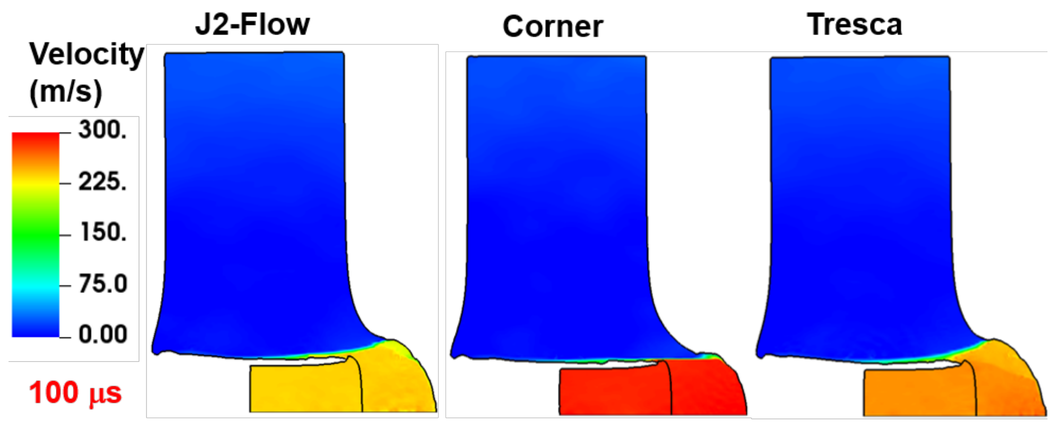

Figure 13. Predicted velocity fields for the J2-flow, corner, and Tresca yield surface models at 100 μs.

3.3 Shear Stress

The velocity differences are tied to the energy dissipated, which is related to the stress state. The shear stress is emphasized here because it is most closely related to the evolution of plugging. Figure 14 shows the shear stress at 60 μs for the three yield functions. As expected, the shear stress emanating from the corner of the projectile for the Tresca material is lower than that of the J2-flow theory material due to the faceted nature of the yield surface. The shear stress for the corner theory material at the same location is intermediate between the others. This is consistent with the velocities shown in Figure 11 where the projectile is moving fastest in the Tresca material. The corner theory solution has a reduced shear stress near the corner of the projectile; this a result of stress release from the failed material at that location.

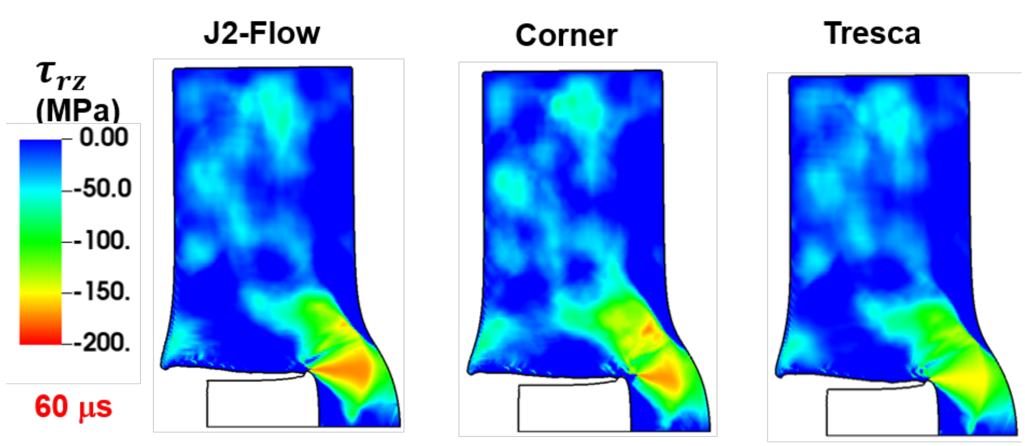

Figure 14. Shear stress fields revealing the elevated shear stress associated with the corner of the projectile for the J2-flow, corner, and Tresca yield surface models at 60 μs.

3.4 Strain and Strain Rate Fields

Strain and strain rate fields are provided to corroborate the inferences from the velocity fields. The effective plastic strain and the plastic strain rate are shown at 60 μs in Figure 15. The strain fields in the upper half of the figure are similar qualitatively and quantitatively at this time, indicating that the particular yield function had not affected the earlier deformation substantially. Plastic strain accumulates ahead of the projectile as it flows radially to expand the cavity.

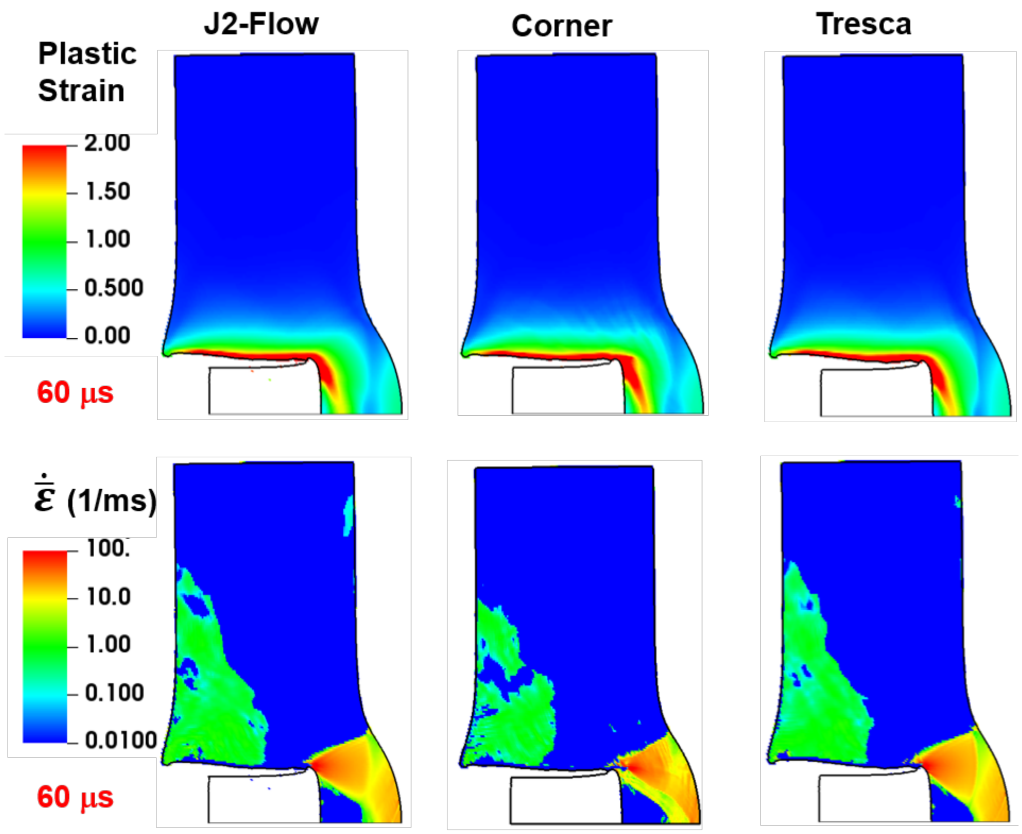

Figure 15. Plots of plastic strain (top row) and plastic strain rate (bottom row) at 60 μs for the J2-flow, corner, and Tresca yield surface models.

The strain rate fields in the lower portion of Figure 15 are also similar in that they have a fan structure originating from the corner of the projectile. That fan of elevated strain rate indicates that the deformation is diffuse and not focused into a band. There is an additional high strain rate area at the front of the bulge on the right of the figures. This is associated with stretching of the bulge. There is a region of lower strain rate between these two features that is simply a lower rate region between two higher rate regions.

The strain rate field from the corner theory model has a band of lower rate below the fan and immediately ahead of the conical slug being pushed by the penetrator.

This band appears to originate at the fracture at the projectile corner, so it is assumed that the feature is related to the fracture.

Strain and strain rate plots at 80 μs are given in Figure 16. The strain fields in the upper portion of the figure are again similar to each other except that the corner theory solution has a horizontal protrusion of high strain at the corner of the projectile. This elevated strain is responsible for the increased damage in that area and the subsequent fracture.

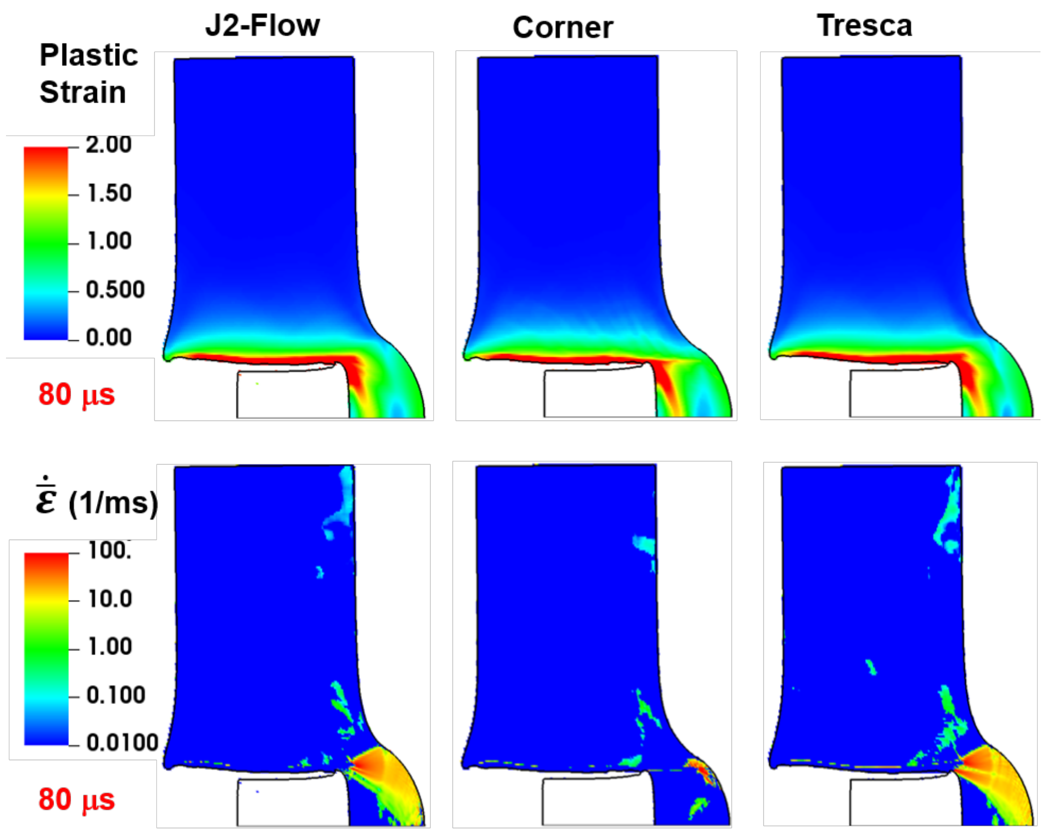

Figure 16. Plots of plastic strain (top row) and plastic strain rate (bottom row) at 80 μs for the J2-flow, corner, and Tresca yield surface models.

The strain rate plots in the lower portion of Figure 16 reveal that the corner theory model has nearly complete failure along the boundary of the plug. A remnant near the free surface has a high strain rate and will quickly reach the damage threshold. The remainder of the plug surface is sliding along a narrow band. The J2-flow and Tresca models continue to show the strain rate fan, indicating sustained diffuse plastic flow at 80 μs. This is consistent with the velocity fields in Figure 12.

3.5 Damage Fields

Figure 17 shows the damage parameter calculated by the Johnson–Cook failure model at 60 and 80 μs for the three yield surface models. The damage pattern deviates somewhat from the plastic strain because of pressure dependence. The elevated plastic strain seen ahead of the penetrator in Figures 15 and 16 does not lead to damage due to the higher pressure in that region. At 60 μs, the corner theory result shows high damage extended from the outer radius of the projectile. Failure in this segment is consistent with the velocity and stress plots. The damage threshold is not exceeded ahead of the penetrator for the J2-flow theory and Tresca results at 60 μs. By 80 μs, the corner theory calculation exhibits a sharp damage line extending to the surface, consistent with plugging. The J2-flow theory and Tresca damage plots indicate damage at the threshold value a small distance ahead of the penetrator corner. This damage provides a stress concentration that accelerates further damage, akin to a shear crack.

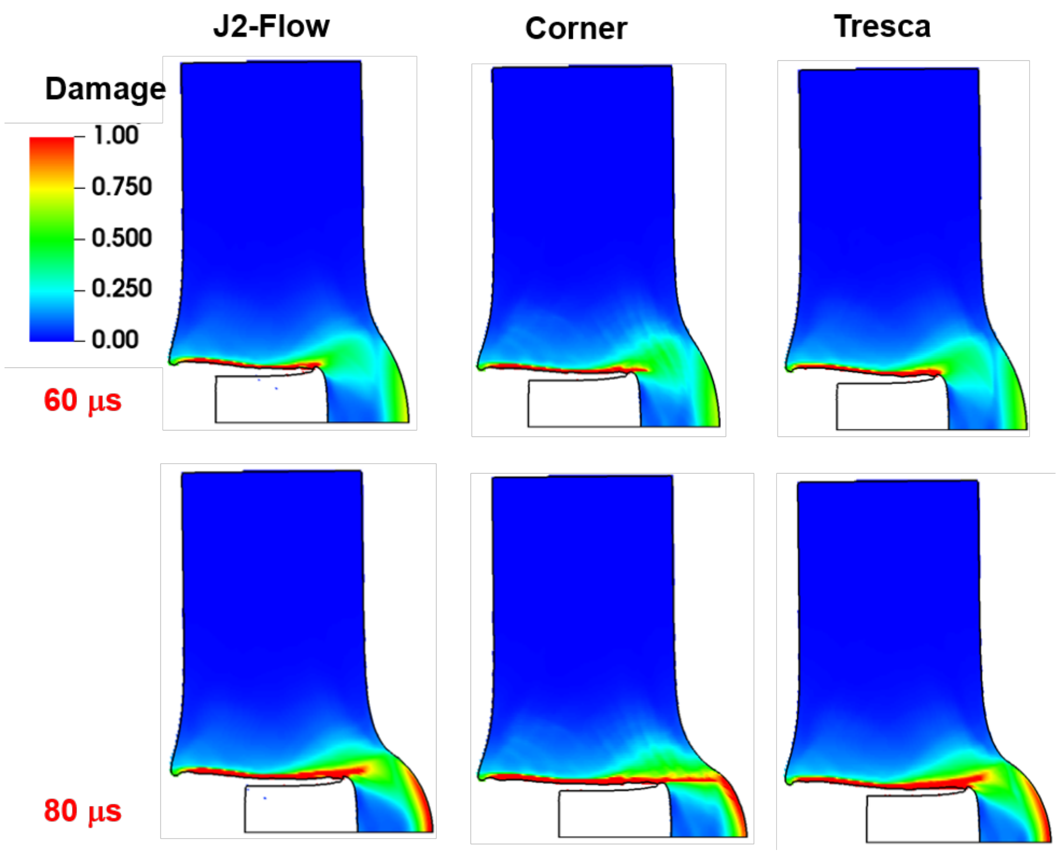

Figure 17. Damage plots at 60 and 80 μs for the J2-flow, corner, and Tresca yield surface models.

4. Summary and Future Work

An analytic solution integrating the J2-flow theory flow potential over a time step has been arranged into a form that scales the strain increment to keep it smaller than the yield strain. This was reinterpreted as a reduced shear modulus that keeps the elastic trial stress within one yield surface radius of the initial stress. The limited trial stress excursion permits specifying viable return plastic flow paths based on conditions at the beginning of the time step. Similar plastic returns from large elastic trial stresses may not intersect the yield surface.

The modulus reduction concept was applied to an existing corner theory model. Verification and validation solutions showed robust and accurate solutions over a broad range of time increments. An example simulation of a steel cylinder impacting an aluminum plate showed agreement with the standard J2-flow theory model during the initial phase of the penetration. At later stages, when the penetrator stress field interacts with the rear surface of the plate, the corner theory model permitted plastic flow localization and plugging.

A Tresca yield surface model with radial return plastic flow was also implemented for comparison. This created a nonassociated flow rule. The lower shear strength from the Tresca surface dissipated less energy in the penetration than the J2-flow model, and the penetration velocity was higher.

Future work for yield functions includes investigating a way to combine a corner theory model with the lower shear strength from the Tresca yield criterion. In addition, concepts of a shear band indicator will be explored in combination with the enhanced localization predictions of the Tresca and corner theory models to improve predictions of strain localization leading to fracture.

5. References

Bassani JL, Racheria V. From non-planar dislocation cores to non-associated plasticity and strain bursts. Prog Mater Sci. 2011;56:852–863. https://doi.org/10.1016/j.pmatsci.2011.01.010

Beissel SR, Gerlach CA. User instruction for the 2025 version of EPIC. Southwest Research Institute; 2025.

Christoffersen J, Hutchinson JW. A class of phenomenological corner theories of plasticity. J Mech Phys Solids. 1979;27:465–487. https://doi.org/10.1016/0022-5096(79)90026-7

Dawson DM et al. ALE3D: an arbitrary Lagrange/Eulerian 2D and 3D code system. Lawrence Livermore National Laboratory (US); 2020. Report No.: LLNL-MI-845330.

Fish J, Belytschko T. Elements with embedded localization zones for large deformation problems. Comp Struct. 1988:30(1-2);247–256. https://doi.org/10.1016/0045-7949(88)90230-1 .

Hecker SS. Experimental studies of yield phenomena in biaxially loaded metals. Annual Meeting of the American Society of Mechanical Engineers; New York, NY; 29 Nov 1976. p. 1–33.

Hill R. The mathematical theory of plasticity. Oxford University Press; 1950. https://doi.org/10.1093/oso/9780198503675.001.0001

Krieg RD, Krieg DB. Accuracies of numerical solution methods for the elastic-perfectly plastic model. J Press Vess Technol Trans ASME. 1977;99(4):510–515. https://doi.org/10.1115/1.3454568

Kuroda M, Tvergaard V. A phenomenological plasticity model with non-normality effects representing observations in crystal plasticity. J Mech Phys Solids. 2001a;49:1239–1263. https://doi.org/10.1016/S0022-5096(00)00080-6

Kuroda M, Tvergaard V. Shear band development predicted by a non-normality theory of plasticity and comparison to crystal plasticity predictions. Int J Solids Struct. 2001b;38:8945–8960. https://doi.org/10.1016/S0020-7683(01)00166-4

Kuwabara T, Kuroda M, Tvergaard V, Nomura K. Use of abrupt strain path change for determining subsequent yield surface: Experimental study with metal sheets. Acta Mater. 2000;48:2071–2079. https://doi.org/10.1016/S1359-6454(00)00048-3

Margraf J, Barton NR. Shear band insertion for capturing strain localization. AIP Conf. Proc. 2019;2272:070031. https://doi.org/10.1063/12.0000889

Mourad HM, Bronkhorst CA, Livescu V, Plohr JN, Cerreta EK. Modeling and simulation framework for dynamic strain localization in elasto-viscolastic metallic materials subject to large deformations. Int J Plast. 2017;88:1–26. https://doi.org/10.1016/j.ijplas.2016.09.009

Murnaghan FD. The compressibility of media under extreme pressures, Proceedings of the National Academy of Sciences of the United States of America. 1944;30(9):244–247. https://doi.org/10.1073/pnas.30.9.244

Press WH, Teukolsky SA, Vettering WT, Flannery BP. Numerical Recipes in Fortran: The Art of Scientific Computing, 2nd ed. Cambridge University Press; 1992.

Raniecki B, Bruhns OT. Bounds to bifurcation stresses with non-associated plastic flow law at finite strain. J Mech Phys Solids. 1981;29(2):153–172. https://doi.org/10.1016/0022-5096(81)90021-1

Rice JR. The localization of plastic deformation. In: Koiter WT, editor. Theoretical and applied mechanics. North Holland Publishing; 1976. p. 207–220.

Sheffield SA, Mitchell DE, Hayes DB. The equation of state and chemical kinetics for Hexanitrostilbene (HNS) explosive. Proceedings of the Sixth Symposium (International) on Detonation, Office of Naval Research, ACR-221, Arlington, VA. 1976:748–754.

Simo JC. A J2-flow theory exhibiting a corner-like effect and suitable for large-scale computation. Comp Meth Appl Mech Engr. 1987;62:169–194. https://doi.org/10.1016/0045-7825(87)90022-3

Triantafyllidis N, Needleman A, Tvergaard V. Development of shear bands in pure bending. Int J Solids Struct. 1982;18(2):121–138. https://doi.org/10.1016/0020-7683(82)90021-X

Wright TW, Walter JW. On stress collapse in adiabatic shear bands. J Mech Phys Solids. 1987;35(6):701–720. https://doi.org/10.1016/0022-5096(87)90051-2

Appendix. Analytic Integration of J2-Flow Relations

The stress rate equation for integrating the J2-flow theory flow potential is

$$\widehat{\boldsymbol{\sigma}}' = 2\mu\, \boldsymbol{d}' - 3\mu\dot{\bar{\varepsilon}}\, \frac{\boldsymbol{\sigma}_t'}{\sigma_t^{vm}} \tag{A-1}$$

The strategy is to break the integral over the single time step, denoted Δt, into N substeps using successive substitution. Since this represents a single macro time step, it is assumed that the stress has already been adjusted for rotational objectivity and that the rate of deformation tensor is constant over the time step. From the rate form, the relation to get from one substep (n) to the next ($n+1$) is

$$\begin{aligned} \boldsymbol{\sigma}'_{t+\frac{n+1}{N}\Delta t} &= \boldsymbol{\sigma}'_{t+\frac{n}{N}\Delta t} + 2\mu\, \boldsymbol{d}' \frac{\Delta t}{N} - \frac{3\mu\dot{\bar{\varepsilon}}}{\sigma_t^{vm}} \frac{\Delta t}{N}\, \boldsymbol{\sigma}'_{t+\frac{n}{N}\Delta t} \\ &= 2\mu\, \boldsymbol{d}' \frac{\Delta t}{N} + \left(1 - \frac{3\mu\dot{\bar{\varepsilon}}}{\sigma_t^{vm}} \frac{\Delta t}{N}\right) \boldsymbol{\sigma}'_{t+\frac{n}{N}\Delta t} \\ &= \boldsymbol{D} + x\boldsymbol{\sigma}'_{t+\frac{n}{N}\Delta t} \end{aligned} \tag{A-2}$$

where variables $\boldsymbol{D}$ and x have been introduced for convenience.

The series begins as

$$\boldsymbol{\sigma}'_{t+\frac{1}{N}\Delta t} = \boldsymbol{D} + x\boldsymbol{\sigma}_t' \ . \tag{A-3}$$

Using the result from the first substep, stress at the end of the second subincrement is

$$\boldsymbol{\sigma}'_{t+\frac{2}{N}\Delta t} = \boldsymbol{D} + x\boldsymbol{\sigma}'_{t+\frac{1}{N}\Delta t} = \boldsymbol{D} + x\boldsymbol{D} + x^2\boldsymbol{\sigma}_t' \,. \tag{A-4}$$

At the end of the third subincrement, the stress is

$$\boldsymbol{\sigma}'_{t+\frac{3}{N}\Delta t} = \boldsymbol{D} + x\boldsymbol{\sigma}'_{t+\frac{2}{N}\Delta t} = \boldsymbol{D} + x\boldsymbol{D} + x^2\boldsymbol{D} + x^3\boldsymbol{\sigma}_t' \,. \tag{A-6}$$

Extrapolating to the stress at the end of N'th sub increment,

$$\boldsymbol{\sigma}'_{t+\frac{N}{N}\Delta t} = \boldsymbol{D} + x\boldsymbol{D} + x^2\boldsymbol{D} + \cdots + x^{N-1}\boldsymbol{D} + x^N\boldsymbol{\sigma}_t' \,. \tag{A-7}$$

The series has closed-form equivalents. The finite sum associated with $\boldsymbol{D}$ is

$$1 + x + x^2 + x^3 + \cdots + x^{N-1} = \frac{1 - x^N}{1 - x} \,. \tag{A-8}$$

The factor x^Nappears both here and as the coefficient on the stress.

Taking the limit as N approaches infinity, $x^N$is

$$x^N = \lim_{N\to\infty}\left(1 - \frac{3\mu\dot{\bar{\varepsilon}}}{\sigma_t^{vm}}\frac{\Delta t}{N}\right)^N = \exp\left(-\frac{3\mu\dot{\bar{\varepsilon}}\Delta t}{\sigma_t^{vm}}\right). \qquad \text{(A-9)}$$

Substituting the longer expressions in for x^N and $\boldsymbol{D}$ into Equation A-7, the stress at the end of the time step is

$$\boldsymbol{\sigma}'_{t+\Delta t} = \exp\left(-\frac{3\mu\dot{\bar{\varepsilon}}\Delta t}{\sigma_t^{vm}}\right)\boldsymbol{\sigma}'_t + \frac{1 - \exp\left(-\frac{3\mu\dot{\bar{\varepsilon}}\Delta t}{\sigma_t^{vm}}\right)}{\frac{3\mu\dot{\bar{\varepsilon}}}{\sigma_t^{vm}}\frac{\Delta t}{N}} 2\mu\,\boldsymbol{d}'\frac{\Delta t}{N}, \qquad \text{(A-10)}$$

which can be simplified to

$$\boldsymbol{\sigma}'_{t+\Delta t} = \exp\left(-\frac{3\mu\dot{\bar{\varepsilon}}\Delta t}{\sigma_t^{vm}}\right)\boldsymbol{\sigma}'_t + \sigma_t^{vm}\left[1 - \exp\left(-\frac{3\mu\dot{\bar{\varepsilon}}\Delta t}{\sigma_t^{vm}}\right)\right]\frac{2\,\boldsymbol{d}'\Delta t}{3\,\dot{\bar{\varepsilon}}\Delta t}. \qquad \text{(A-11)}$$

The assumptions, constraints, and final functional form from this approach differ from those of Krieg and Krieg.[1] Their final stress was constrained to lie on the original yield surface, and the argument of the exponential in their solution is the stress increment. The solution did not involve the plastic strain rate. In the current development, only the von Mises stress normalizing $3\mu\dot{\bar{\varepsilon}}\Delta t$ is assumed constant. There is no constraint requiring the stress to return to the initial yield surface. The final stress is a function of the plastic strain rate.

[1] Krieg RD, Krieg DB. Accuracies of numerical solution methods for the elastic-perfectly plastic model. J Press Vess Technol Trans ASME. 1977;99(4):510–515. https://doi.org/10.1115/1.3454568

List of Symbols, Abbreviations, and Acronyms

ARL	Army Research Laboratory
DEVCOM	U.S. Army Combat Capabilities Development Command
DoW	Department of War
EOS	Equation of State
α	Adjustment to corner theory angle
c	Flow stress dependent factor for corner theory model
c_v	Specific heat
$\boldsymbol{d}'$	Deviatoric part of the rate of deformation tensor
F(v)	Murnaghan energy function
$\mathcal{F}(v,T)$	Helmholtz energy function
K	Bulk modulus
k'	Pressure derivative of the bulk modulus
$\mathcal{M}$	Shear modulus reduction factor
$\boldsymbol{m}$	Direction orthogonal to applied strain rate
$\boldsymbol{n}$	Yield surface normal
$\boldsymbol{P}$	Generic plastic flow direction
$\mathcal{R}$	Quantity approximately equal to multiples of the yield strain
$\tilde{\mathcal{S}}$	Entropy per unit reference volume
T	Absolute temperature
$\tilde{\mathcal{U}}(V,\tilde{\mathcal{S}})$	Internal energy per unit reference volume
v	Specific volume
V	Relative volume
Δt	Time increment
$\dot{\varepsilon}$	Equivalent plastic strain rate
$\dot{\boldsymbol{\varepsilon}}'^{p}$	Deviatoric part of the plastic strain rate

$\dot{\epsilon}$	Approximated strain rate use in modulus reduction
μ	Shear modulus
$\mu *$	Reduced shear modulus
ϕ	Yield function
θ	Angle between surface normal and applied strain rate
θ_{crit}	Critical angle for corner theory model
$\bar{\sigma}(\bar{\varepsilon}, \dot{\bar{\varepsilon}}, T, p, \ldots)$	Material strength
$\widehat{\boldsymbol{\sigma}}'$	Objective rate of the deviatoric part of the Cauchy stress tensor
$\boldsymbol{\sigma}_{\boldsymbol{t}}'$	Deviatoric part of the Cauchy stress tensor at time t.
$\boldsymbol{\sigma}^T$	Trial stress
σ_t^{vm}	Von Mises equivalent stress at time t.
σ_{eff}^T	Effective trial stress
σ_{Aux}	Auxiliary variable with units of stress
ρ	Density
Γ	Grüneisen coefficient

1 (PDF)	DEFENSE TECHNICAL INFORMATION CTR DTIC OCA
1 (PDF)	DEVCOM ARL FCDD RLB CB TECH LIB